Convective dynamos in spherical wedge geometry

P.J. Käpylä[1,2,*], **M.J. Korpi**[1], **A. Brandenburg**[2,3], **D. Mitra**[4], and **R. Tavakol**[4]

[1] Observatory, University of Helsinki, PO BOX 14, FI-00014 University of Helsinki, Finland

[2] NORDITA, AlbaNova University Center, Roslagstullsbacken 23, SE-10691 Stockholm, Sweden

[3] Department of Astronomy, AlbaNova University Center, Stockholm University, SE-10691 Stockholm, Sweden

[4] Astronomy Unit, School of Mathematical Sciences, Queen Mary University of London, Mile End Road, London E1 4NS, United Kingdom

Self-consistent convective dynamo simulations in wedge-shaped spherical shells are presented. Differential rotation is generated by the interaction of convection with rotation. Equatorward acceleration and dynamo action are obtained only for sufficiently rapid rotation. The angular velocity tends to be constant along cylinders. Oscillatory large-scale fields are found to migrate in the poleward direction. Comparison with earlier simulations in full spherical shells and Cartesian domains is made.

1 Introduction

The large-scale magnetic fields in the Sun and other stars are thought to arise from a complex interplay between nonuniform rotation, stratification, and convective turbulence (e.g. Ossendrijver 2003; Brandenburg & Subramanian 2005). According to mean-field theory of turbulent dynamos, one of the main mechanisms responsible for the generation of large-scale fields is the α effect, which is related to the kinetic helicity of the flow in idealised cases (Moffatt 1978; Krause & Rädler 1980; Rüdiger & Hollerbach 2004). In the simplest settings, kinetic helicity is produced by rotating inhomogeneous turbulence. The inhomogeneity can arise from density stratification, or, in the absence of stratification, from impenetrable boundaries. However, although many early numerical simulations of rotating convection did work as dynamos (e.g. Nordlund et al. 1992; Brandenburg et al. 1996), the magnetic field generated in these models was found to be mostly on small scales, with the typical spatial scale of the field of the same order as the typical size of convection cells. This posed a puzzle, given that the simulations included all the major ingredients (stratification and rotation) known to be necessary for the α effect to occur. Crucial insight into this problem was gained when the test-field method (Schrinner et al. 2005, 2007) was used to compute the relevant turbulent transport coefficients (Käpylä et al. 2009b). It was found that the α effect resulting from the relatively slow rotation used in the earlier studies was not enough to overcome turbulent diffusion. On the other hand, for more rapid rotation, turbulent diffusion was found to decrease which, according to mean-field models, would imply that large-scale dynamo action should become pos-

sible. This was recently confirmed by direct simulations in the same parameter regime (Käpylä et al. 2009a). Similar results had been obtained earlier in the geodynamo context (e.g. Jones & Roberts 2000; Rotvig & Jones 2002), but subsequent simulations by Cattaneo & Hughes (2006) suggested that large-scale field generation becomes impossible at larger magnetic Reynolds numbers. However, this is now believed to be a consequence of rotation being too slow (Käpylä et al. 2009a).

Furthermore, during the last few years simulations have verified that shear can be the sole driver of large-scale dynamo action in non-helical turbulence (Yousef et al. 2008a,b; Brandenburg et al. 2008). The shear-current effect (Rogachevskii & Kleeorin 2003, 2004) has been proposed as a mechanism responsible for the dynamo, but the details of the numerical results disagree in various respects with the theoretical expectations. This numerical finding provided a motivation to add large-scale shear into a convective system (Käpylä et al. 2008, 2009c; Hughes & Proctor 2009). As a result it was found that these models indeed yield strong large-scale dynamos, but their theoretical interpretation in terms of mean-field theory is not as clear as in the case where only rotation is present (Käpylä et al. 2009b).

Local simulations can be used to demonstrate the existence of a large-scale dynamo and the processes that are responsible for the generation of the magnetic fields can be more readily studied. However, they cannot be used to study the global behaviour of solar and stellar dynamos, which occur in spherical geometry and generate a much richer variety of physical effects. Furthermore, the large-scale flows that need to be imposed in the local models can arise self-consistently in the spherical models.

* Corresponding author: petri.kapyla@helsinki.fi

Simulations of convective dynamos in spherical geometry have a long history starting from the seminal papers of Gilman (1983) and Glatzmaier (1985), to the present (e.g. Brun et al. 2004; Browning et al. 2006; Brown et al. 2007, 2009). These models are now quite advanced and, with suitable boundary conditions, are capable of reproducing the solar internal rotation profile (e.g. Miesch et al. 2006). However, no cyclic large-scale dynamos have so far been discovered in models of the solar convection zone (e.g. Brun et al. 2004; Browning et al. 2006). On the other hand, models of rapidly rotating stars do exhibit significant large-scale magnetic fields (Brown et al. 2007, 2009), although none of these studies has yet been able to produce poleward propagating dynamo waves first observed by Gilman (1983), or anything akin to the solar cycle.

Modelling a full convection zone in a spherical shell though clearly desirable, has an important drawback, with the spatial resolution achieved in such simulations being inevitably lower than in models that encompass only a part of the shell. One can also argue that it may not be necessary to model the full latitudinal and longitudinal extents of the convection zone in order to capture the essential physics of the solar dynamo. Main arguments to justify this approach are that the solar magnetic activity appears to be concentrated in a latitude range of $\pm 40°$ around the equator and that the large-scale field is mostly axisymmetric. This has recently motivated simulations of forced turbulence in parts ('wedges') of full spherical shells (Brandenburg et al. 2007; Mitra et al. 2009a,b). These simulations aim to strike a reasonable compromise between the requirements of higher spatial resolution on the one hand and globality on the other. Convection simulations in wedge-shaped geometry have already been performed by Robinson & Chan (2001) and DeRosa & Hurlburt (2003). Those simulations, however, did not include magnetic fields. In the present paper we report preliminary results of convection-driven dynamos in spherical wedge-geometry.

2 Model

The simulations reported here are performed in spherical polar coordinates where (r, θ, ϕ) denote radius, colatitude, and the azimuth, respectively (in some of our space-time diagrams, e.g. Fig. 7, we use the latitude $\Theta = 90° - \theta$.) As our domain we consider, instead of a full spherical shell, a spherical wedge that spans $0.6R \leq r \leq R$ in radius (where R is the outer radius of the sphere which is also used as our unit length), $-\Delta\Theta < \Theta < \Delta\Theta$ in latitude, and $0 < \phi < \Delta\phi$ in longitude. We then solve the following set of compressible magnetohydrodynamic equations for the magnetic vector potential $\boldsymbol{A}$ (which is related to the magnetic field $\boldsymbol{B}$ by $\boldsymbol{B} = \boldsymbol{\nabla} \times \boldsymbol{A}$), the logarithmic density $\ln\rho$, the velocity $\boldsymbol{U}$, and the specific entropy s:

$$\frac{D\boldsymbol{A}}{Dt} = \boldsymbol{U} \times \boldsymbol{B} - \mu_0\eta\boldsymbol{J}, \tag{1}$$

$$\frac{D\ln\rho}{Dt} = -\boldsymbol{\nabla}\cdot\boldsymbol{U}, \tag{2}$$

$$\frac{D\boldsymbol{U}}{Dt} = \boldsymbol{g} - 2\boldsymbol{\Omega}\times\boldsymbol{U} + \frac{1}{\rho}\left(\boldsymbol{J}\times\boldsymbol{B} - \boldsymbol{\nabla}p + \boldsymbol{\nabla}\cdot 2\nu\rho\boldsymbol{\mathsf{S}}\right), \tag{3}$$

$$T\frac{Ds}{Dt} = \frac{1}{\rho}\boldsymbol{\nabla}\cdot K\boldsymbol{\nabla}T + 2\nu\boldsymbol{\mathsf{S}}^2 + \frac{\mu_0\eta}{\rho}\boldsymbol{J}^2, \tag{4}$$

where $D/Dt = \partial/\partial t + \boldsymbol{U}\cdot\boldsymbol{\nabla}$ is the advective derivative, and $\boldsymbol{J} = \mu_0^{-1}\boldsymbol{\nabla}\times\boldsymbol{B}$ is the current density. The vacuum permeability is given by μ_0, whereas magnetic diffusivity and kinematic viscosity are given by η and ν, respectively. The rotation vector is given by $\boldsymbol{\Omega} = \Omega_0(\cos\theta, -\sin\theta, 0)$, where Ω_0 is the constant rotation rate of the frame. For simplicity, we have ignored the centrifugal force, as it is a second order effect in Ω; see Dobler et al. (2006) for a more detailed justification. The gravitational acceleration, $\boldsymbol{g}$, is given by

$$\boldsymbol{g} = -\frac{GM}{r^2}\hat{\boldsymbol{r}}, \tag{5}$$

where G is the universal constant of gravitation, M is the mass of the star, and $\hat{\boldsymbol{r}}$ is a unit vector in the radial direction. The fluid obeys an ideal gas law $p = \rho e(\gamma - 1)$, where p and e are the pressure and internal energy, respectively, and $\gamma = c_P/c_V = 5/3$ is the ratio of specific heats at constant pressure and volume. The heat conductivity is given by K and the internal energy is related to the temperature via $e = c_V T$. The specific entropy is given by

$$s = c_V \ln(p/p_0) - c_P \ln(\rho/\rho_0), \tag{6}$$

where p_0 and ρ_0 are constants defined below. The temperature can now be written as

$$T = T_0 \exp\left[\gamma\frac{s}{c_P} + (\gamma - 1)\ln\left(\frac{\rho}{\rho_0}\right)\right], \tag{7}$$

where $T_0 = p_0/[c_V\rho_0(\gamma - 1)]$.

The rate of strain tensor $\boldsymbol{\mathsf{S}}$ is given by

$$\mathsf{S}_{ij} = \tfrac{1}{2}(U_{i;j} + U_{j;i}) - \tfrac{1}{3}\delta_{ij}\boldsymbol{\nabla}\cdot\boldsymbol{U} \tag{8}$$

where ';' denotes covariant differentiation (see Mitra et al. 2009a, for more details). We consider a setup where the stratification in the region below $r = 0.7R$ is convectively stable, whereas the region above is unstable. The positions of the bottom of the domain, bottom of the convectively unstable layer, and the top of the domain are given by $(r_1, r_2, r_3) = (0.6, 0.7, 1)R$. The setup yields a hydrostatic equilibrium temperature

$$T(r) = T_3 + \int_{r_3}^{r}\frac{|\boldsymbol{g}|}{c_V(\gamma - 1)(m + 1)}dr, \tag{9}$$

where T_3 is the temperature at r_3 and where $m = m(r)$ is chosen to have a suitable radial profile. This procedure gives a temperature stratification for which the logarithmic temperature gradient (not to be confused with the gradient operator $\boldsymbol{\nabla}$) is given by

$$\nabla \equiv \partial\ln T/\partial\ln p = (m + 1)^{-1}, \tag{10}$$

The stratification is convectively unstable when $\nabla - \nabla_{\mathrm{ad}} > 0$, where $\nabla_{\mathrm{ad}} = 1 - 1/\gamma$. Thus m can be considered as a polytropic index, with values $m < 1.5$ yielding an unstable stratification. We choose $m = 1$ in the convectively

unstable layer ($r > r_2$) and $m = 3$ in the stable layer below ($r_1 < r < r_2$) with a smooth transition in between. The density stratification is obtained by requiring the hydrostatic equilibrium condition to be satisfied.

The thermal conductivity is obtained by requiring a constant luminosity L throughout the domain via

$$K = \frac{L}{4\pi r^2 \partial T/\partial r}. \tag{11}$$

In order to speed up thermal relaxation, we use $m = 1$ only for the thermal conductivity profile, whereas the actual thermal stratification of the thermodynamic variables followed a shallower profile with $\rho \sim T^{1.4}$. The initial non-convecting stratification is shown in Fig. 1. A fixed temperature gradient is imposed at the base of the domain which leads to a constant flux of energy into the domain. At the outer radial boundary the temperature is kept constant and on the latitudinal boundaries we set $\partial_\theta T = 0$ so that there is no heat flux in or out of the domain.

For the velocity, the upper radial and the latitudinal boundaries are taken to be impenetrable and stress free, whereas at the lower boundary rigid rotation is enforced by taking

$$U_r = U_\phi = 0, \frac{\partial U_\theta}{\partial r} = \frac{U_\theta}{r} \qquad (r = r_1), \tag{12}$$

$$U_r = 0, \frac{\partial U_\theta}{\partial r} = \frac{U_\theta}{r}, \frac{\partial U_\phi}{\partial r} = \frac{U_\phi}{r} \qquad (r = r_3), \tag{13}$$

$$\frac{\partial U_r}{\partial \theta} = U_\theta = 0, \frac{\partial U_\phi}{\partial \theta} = U_\phi \cot\theta \qquad (\theta = \theta_1, \theta_2), \tag{14}$$

where $\theta_1 = 90° - \Delta\Theta$ and $\theta_2 = 90° + \Delta\Theta$. We use perfect conductor boundary conditions for the magnetic field at the lower radial and latitudinal boundaries, and a normal-field condition on the radial top boundary. In terms of the magnetic vector potential these translate to

$$\frac{\partial A_r}{\partial r} = A_\theta = A_\phi = 0 \qquad (r = r_1), \tag{15}$$

$$A_r = 0, \frac{\partial A_\theta}{\partial r} = -\frac{A_\theta}{r}, \frac{\partial A_\phi}{\partial r} = -\frac{A_\phi}{r} \quad (r = r_3), \tag{16}$$

$$A_r = \frac{\partial A_\theta}{\partial \theta} = A_\phi = 0 \qquad (\theta = \theta_1, \theta_2). \tag{17}$$

Finally, all quantities are taken to be periodic in the azimuthal direction.

The simulations were performed using the PENCIL CODE[1], which uses sixth-order explicit finite differences in space and a third-order accurate time stepping method (see Mitra et al. (2009a) for further information regarding the adaptation of the PENCIL CODE to spherical coordinates). We use grid sizes of $64 \times 192 \times 128$ (Runs A1–A4) and 64×256^2 (Run B1) where the angular extent, $2\Delta\Theta \times \Delta\phi$, is either $2 \times 67.5° \times 90°$ or $2 \times 60° \times 120°$; see Table 1 below. Typical snapshots of the radial velocity U_r for the two domain sizes are shown in Fig. 2.

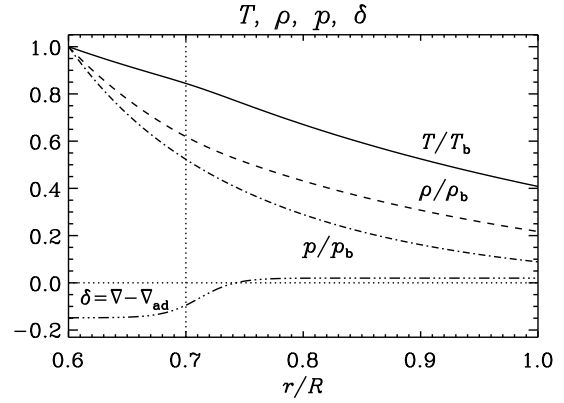
[1] http://pencil-code.googlecode.com/

Fig. 1 Initial stratification of temperature (solid line), density (dashed), pressure (dot-dashed), and the superadiabatic temperature gradient (dash-triple-dotted). The subscripts b refer to the values at $r = r_1$.

2.1 Units, nondimensional quantities, and parameters

Dimensionless quantities are obtained by setting

$$R = GM = \rho_0 = p_0 = c_P = \mu_0 = 1, \tag{18}$$

where ρ_0 is the density at r_1. The units of length, time, velocity, density, entropy, and magnetic field are then given by

$$[x] = R, \quad [t] = \sqrt{R^3/GM}, \quad [U] = \sqrt{GM/R},$$
$$[\rho] = \rho_0, \quad [s] = c_P, \quad [B] = \sqrt{\rho_0\mu_0 GM/R}. \tag{19}$$

The simulations are now governed by the dimensionless Prandtl, Reynolds, Rayleigh and Coriolis numbers defined by

$$\text{Pr} = \frac{\nu}{\chi_0}, \quad \text{Pm} = \frac{\nu}{\eta}, \tag{20}$$

$$\text{Re} = \frac{u_{\text{rms}}}{\nu k_{\text{f}}}, \quad \text{Rm} = \frac{u_{\text{rms}}}{\eta k_{\text{f}}} = \text{Pm}\,\text{Re}, \tag{21}$$

$$\text{Ra} = \frac{GM(r_3 - r_2)^4}{\nu\chi_0 R^2}\left(-\frac{1}{c_P}\frac{ds}{dr}\right)_{r_{\text{m}}}, \tag{22}$$

$$\text{Co} = \frac{2\,\Omega_0}{u_{\text{rms}}k_{\text{f}}}, \tag{23}$$

where $\chi_0 = K/(\rho_{\text{m}}c_P)$ is the thermal diffusivity, $k_{\text{f}} = 2\pi/(r_3 - r_2)$ is an estimate of the wavenumber of the energy-carrying eddies, ρ_{m} is the density in the middle of the unstable layer at $r_{\text{m}} = \frac{1}{2}(r_3 - r_2)$, and u_{rms} is the volume averaged rms velocity. The entropy gradient, measured at r_{m} in the non-convecting initial state, is given by

$$\left(-\frac{1}{c_P}\frac{ds}{dr}\right)_{r_{\text{m}}} = \frac{\nabla_{\text{m}} - \nabla_{\text{ad}}}{H_P}, \tag{24}$$

where $\nabla_{\text{m}} = (\partial \ln T/\partial \ln p)_{r_{\text{m}}}$, and H_P is the pressure scale height at r_m.

The energy that is deposited into the domain from the base is controlled by the luminosity parameter

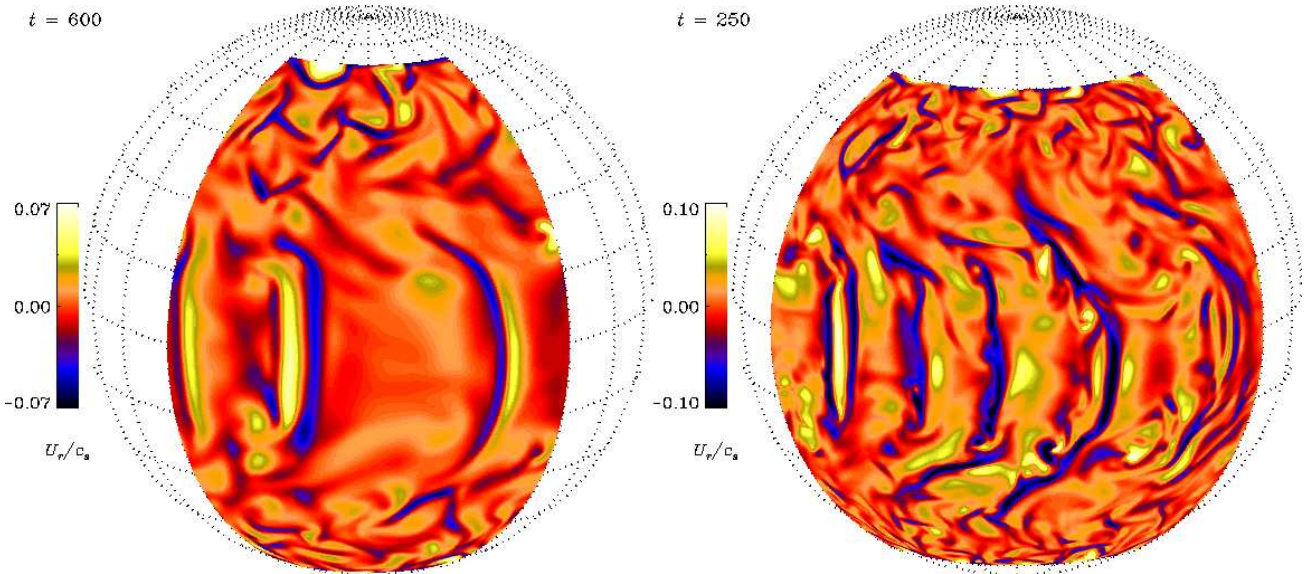$$\mathcal{L} = \frac{L}{\rho_0(GM)^{3/2}R^{1/2}}. \tag{25}$$

Fig. 2 (online colour at: www.an-journal.org) Radial velocity U_r near the upper boundary ($r = 0.98R$) from Runs A4 (left) and B1 (right). The slices are projected onto a spherical surface which is tilted $15°$ towards the observer. The dotted lines in the background show a grid in latitude and longitude in increments of $15°$. See also `http://www.helsinki.fi/~kapyla/movies.html`

Table 1 Summary of the runs. Rm and Co are given in the saturated state of the dynamo. Pm = 1 in all runs.

Run	Rm	Co	Pr	Ra	$\mathcal{L}$	ξ
A1	36	0	0.2	$1.2 \cdot 10^5$	10^{-3}	0.084
A2	71	0.3	0.2	$1.2 \cdot 10^5$	10^{-3}	0.084
A3	35	1.3	0.2	$1.2 \cdot 10^5$	10^{-3}	0.084
A4	28	2.5	0.2	$1.2 \cdot 10^5$	10^{-3}	0.084
B1	45	5.5	0.67	$2.6 \cdot 10^6$	$1.2 \cdot 10^{-4}$	0.078

Furthermore, the stratification is determined by the pressure scale height at the surface

$$\xi = \frac{c_{\mathrm{V}}(\gamma - 1)T_3}{GM/R}. \tag{26}$$

Similar parameter definitions were used earlier by Dobler et al. (2006). The parameter values used in our runs are listed in Table 1.

3 Results

3.1 Hydrodynamic solutions

Before discussing our results with magnetic fields we briefly describe a limited range of hydrodynamic solutions. One of the most important reasons for using spherical geometry is that large-scale shear and meridional flows can be generated self-consistently when the overall rotation of the star is included. In such a setting the kinetic helicity is also likely to vary as a function of position. At large magnetic Reynolds numbers, this information can then be used as a proxy of the trace of the α tensor of mean-field dynamo theory (e.g. Rädler 1980). In order to study the effects of rotation on the flow, we study here a range of models where the rotation rate is gradually increased.

Figure 3 shows cross-sections of longitudinal and temporal averages of the meridional velocities, rotation profile, and kinetic helicity for the kinematic stages of the simulations, from three runs with varying degrees of rotational influence. In the absence of rotation (Run A1), the meridional velocity components show a large-scale structure which is related to long-lived convective cells. However, as there is no mean rotation, no differential rotation is generated in this case, and, although the kinetic helicity $\overline{\boldsymbol{\omega} \cdot \boldsymbol{u}}$ shows fairly large peak values, there is no systematic component present. These results are in accordance with theoretical considerations for nonrotating convection.

When rotation is relatively weak, with Co $\approx$ 0.3 (Run A2), very strong differential rotation and meridional flow is generated. The resulting differential rotation is anti-solar, i.e. the equator is rotating slower than the high-latitude regions. The difference between minimum and maximum rotation rates is remarkably large – about twice the rotation rate of the star. The meridional circulation is also very strong and oriented anti-clockwise. A similar result has been reported by Robinson & Chan (2001) for their convection simulations in a wedge-shaped domain. However, in their case the rotation profile changed to a more solar-like configuration when the longitudinal extent of the domain was doubled. We have not experimented with increasing the ϕ-extent, but we note that there are some other differences; for example, our domain is wider in longitude than that of Robinson & Chan (2001). The kinetic helicity in this case shows signs of large-scale structure: in the northern hemisphere there appears to be positive helicity near the equator and negative helicity at higher latitudes. A similar profile, but with opposite sign, is discernible in the southern hemisphere. The strongest features appear near the lat-
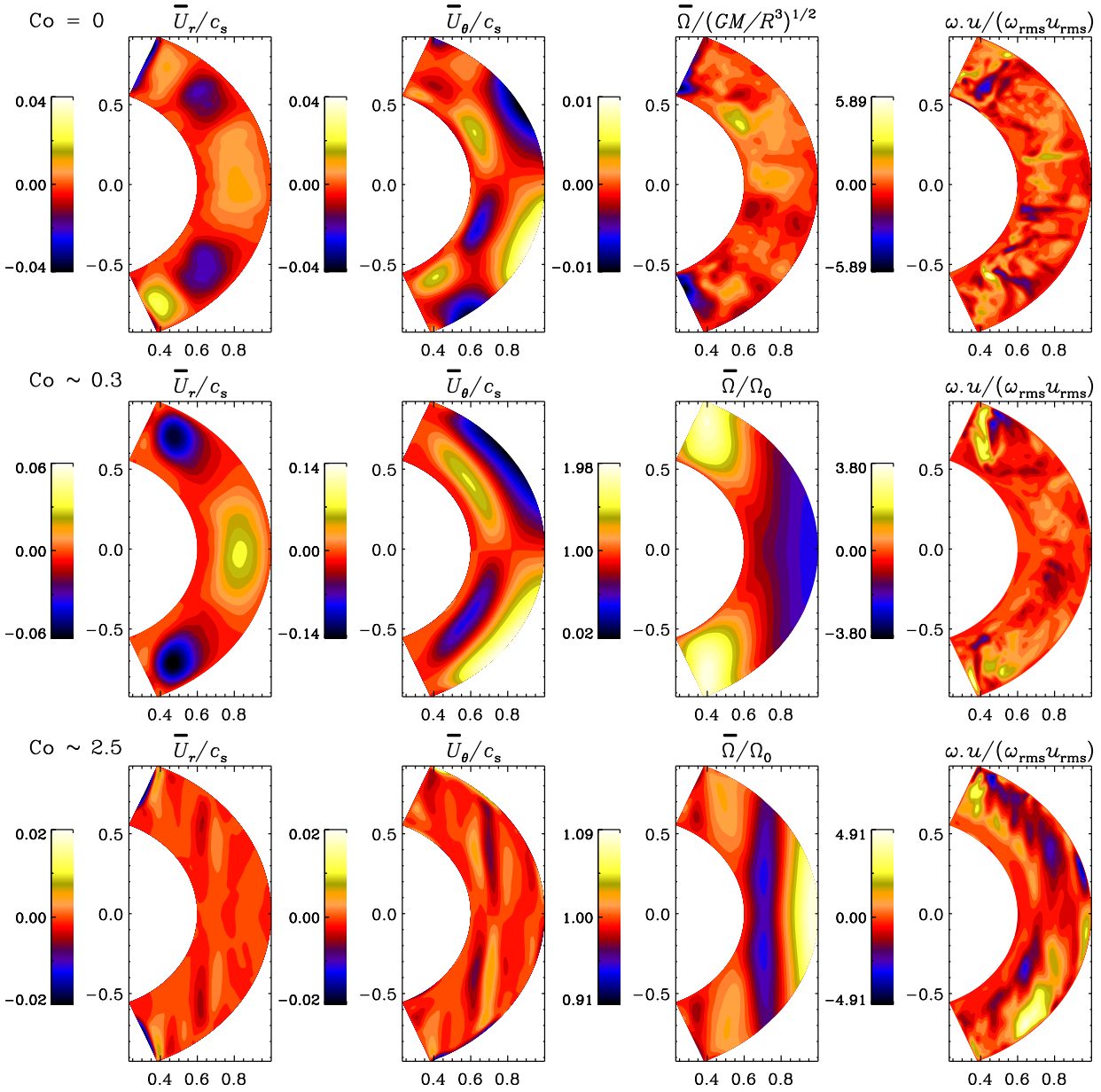
Fig. 3 (online colour at: www.an-journal.org) From left to right: azimuthally averaged $\overline{U}_r$, $\overline{U}_\theta$, $\overline{\Omega} = \overline{U}_\phi/(r\sin\theta) + \Omega_0$, and kinetic helicity $\overline{\boldsymbol{\omega}\cdot\boldsymbol{u}}$ from runs with Co $= 0$ (top row, Run A1), Co ≈ 0.3 (middle, Run A2) and Co ≈ 2.5 (bottom, Run A4) from the kinematic stages of the simulations. Here $\omega_{\rm rms}$ is the rms-value of the vorticity, $\boldsymbol{\omega} = \boldsymbol{\nabla}\times\boldsymbol{u}$.

itudinal boundaries and are possibly due to the converging large-scale flows that occur there.

In the rapidly rotating case with Co ≈ 2.5 (Run A4) the relative differential rotation is significantly reduced and equatorial acceleration is observed. However, the absolute value of $\mathrm{d}\Omega/\mathrm{d}r$, relevant for the large-scale dynamo, is of the same order of magnitude, or somewhat larger near the equator, than in Run A2 with Co ≈ 0.3. In agreement with earlier simulations of convection in rotating spherical shells (e.g., Miesch et al. 2000) the rapid rotation regime is dominated by large prograde 'banana cells' in the radial velocity; see Fig. 2. In our most rapidly rotating models we also see nonaxisymmetric structures in the equatorial regions.

Brown et al. (2008) described such structures as 'nests' of convection. The strength of convection in those structures varies periodically in time and the maxima coincide with enhanced differential rotation similarly as reported by Busse (2002). The left panel of Fig. 2 shows indications of localised convection whereas in the higher Rayleigh number model (Run B1, right panel) these features have not yet developed. We also find that these localised convection structures are suppressed when magnetic fields of equipartition strength are present. The contours of constant Ω are aligned with the rotation vector, in accordance with the Taylor–Proudman balance

$$\frac{\partial\Omega^2}{\partial z} \approx 0, \tag{27}$$

where the z derivative is evaluated as

$$\frac{\partial}{\partial z} = \cos\theta \frac{\partial}{\partial r} - \frac{\sin\theta}{r}\frac{\partial}{\partial \theta}. \tag{28}$$

Only weak meridional circulation is observed and the flow consists of several small cells. This can also be attributed to the Taylor-Proudman balance and has also been found in mean-field calculations (Brandenburg et al. 1991). In the present models the Taylor–Proudman balance always dominates the rotation profile in the rapid rotation regime. Preliminary results from a run with roughly 20 times higher Rayleigh number (Run B1) with Co ≈ 5.5 gives qualitatively very similar results. Reproducing the solar rotation profile self-consistently without resorting to an imposed temperature difference between the equator and the pole (e.g. Miesch et al. 2006) or including unresolved turbulent convective heat fluxes (e.g. Durney & Roxburgh 1971; Kitchatinov et al. 1994; Rüdiger et al. 2005) is likely to be difficult.

We enforce rigid rotation at the lower boundary at $r = 0.6\,R$, although this is unphysical and not even enough to avoid spreading the differential rotation into the stably stratified layer below the convection zone between $r = 0.6\,R$ and $r = 0.7\,R$ (see also Miesch et al. 2000). This spreading is due to the viscosity which is much larger in our simulations than in the solar convection zone. Thus, no tachocline forms in our models. It is also likely that a self-consistent formation of a tachocline requires such high numerical resolution that the problem cannot be tackled successfully in the foreseeable future. A more practical solution is probably the damping of the velocities in the overshoot region, similarly as in Browning et al. (2006).

We also find that in the most rapidly rotating case considered here, the kinetic helicity has a well-defined profile with a mostly negative (positive) value in the northern (southern) hemisphere in the outer layers of the convectively unstable layer. Furthermore, there is a sign change as a function of radius near the base of the convection zone. These results are in accordance with theoretical considerations and earlier results from local and global simulations (e.g. Miesch et al. 2000; Brun et al. 2004; Käpylä et al. 2006). The simple first-order smoothing relation that is valid for isotropic turbulence states that $\alpha \propto -\overline{\boldsymbol{\omega}\cdot\boldsymbol{u}}$ which suggests that the α effect should in the present case have a positive (negative) value in the northern (southern) hemisphere. This will be examined in more detail in the next section.

3.2 Dynamo solutions

We begin our study of dynamo excitation with a model with Rm ≈ 36 that does not act as a dynamo in the absence of rotation (Co $= 0$). For Co ≈ 0.2 the magnetic field shows exponential growth. The time averaged growth rate of the magnetic field,

$$\lambda = \langle \mathrm{d}\ln B_{\mathrm{rms}}/\mathrm{d}t\rangle_t, \tag{29}$$

increases with rotation for small values of Co, see Fig. 4, although it shows a dip at Co ≈ 2.5.
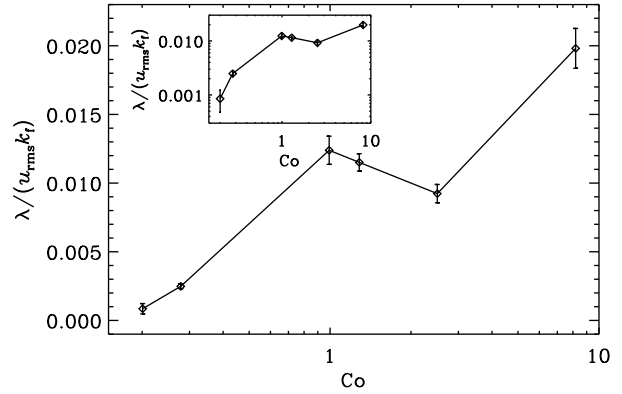

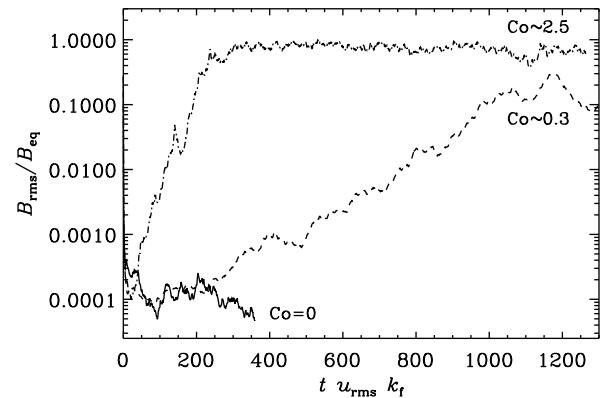**Fig. 4** Growth rate of the magnetic field as a function of rotation.

Fig. 5 Root mean square value of the magnetic field as a function of time for runs with Co $= 0$ (solid line, Run A1), Co ≈ 0.3 (dashed, Run A2), and Co ≈ 2.5 (dash-dotted, Run A4).

In the slowly rotating cases (Co $\lesssim 0.3$) the saturation level of the magnetic field is rather low, $B_{\mathrm{rms}}/B_{\mathrm{eq}} \approx 0.1$, where $B_{\mathrm{eq}} = \sqrt{\mu_0\rho u_{\mathrm{rms}}^2}$ is the equipartition field strength (see Fig. 5). Furthermore, there is a large-scale axisymmetric component to the field which is thus well described by a longitudinal average. In Run A2 with Co ≈ 0.3 the large-scale field is approximately antisymmetric with respect to the equator and shows irregular sign changes on a long time scale (see the upper panel of Fig. 6).

As the rotation rate is increased the qualitative character of the differential rotation changes from anti-solar to solar-like, as was seen in the previous section. A qualitative change occurs also in the behaviour of the dynamo so that for Co ≈ 1.3 (Run A3) magnetic fields of the order of the equipartition strength are obtained. Furthermore, the fields show a large-scale pattern that stays roughly independent of time, i.e. no sign changes are found. However, near the surface there are indications of a time-variable large-scale structure (lower panel of Fig. 6). When the rotation rate is doubled (Co ≈ 2.5, Run A4), the magnetic field indeed shows oscillatory behaviour near the equator, see Figs. 7 and 9, with branches of magnetic fields appearing to move from the equator towards higher latitudes. We interpret the phenomenon as a dynamo wave propagating towards the poles. More precisely, assuming that the sign of the α effect is op-
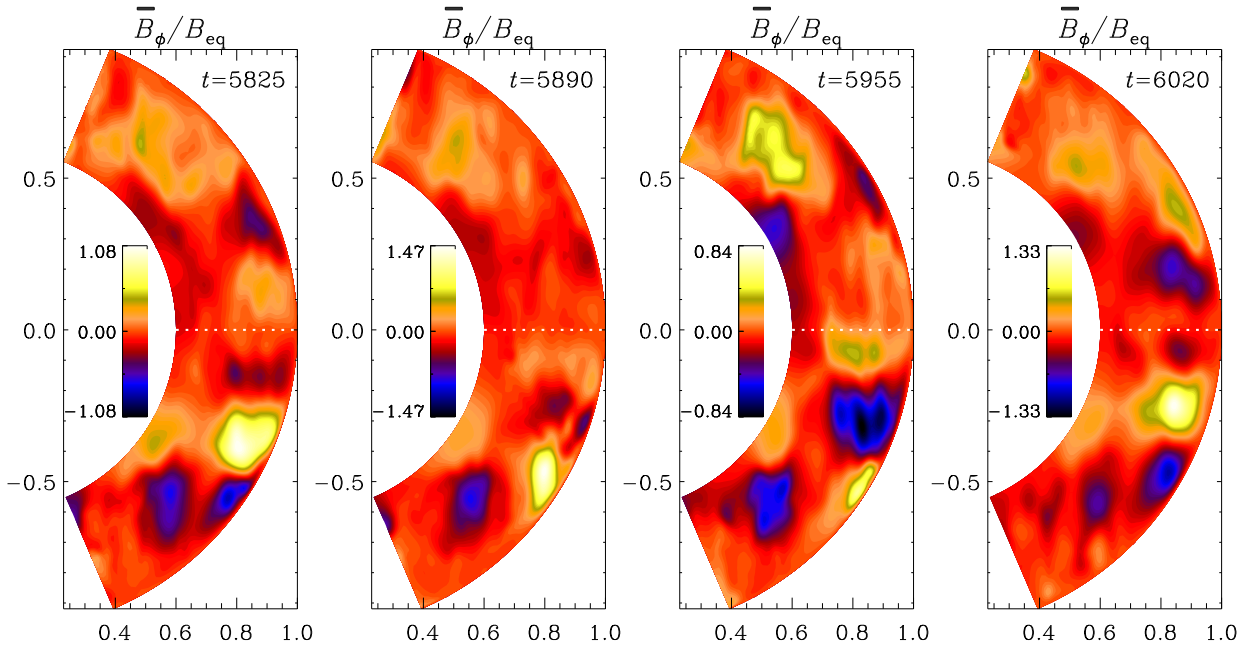
Fig. 8 (online colour at: www.an-journal.org) Azimuthally averaged magnetic field component $\overline{B}_\phi$ from four times separated by $\Delta t = 65\sqrt{R^3/GM}$, corresponding to $\Delta t u_{\rm rms} k_{\rm f} \approx 41$, from Run A4 with Co ≈ 2.5.
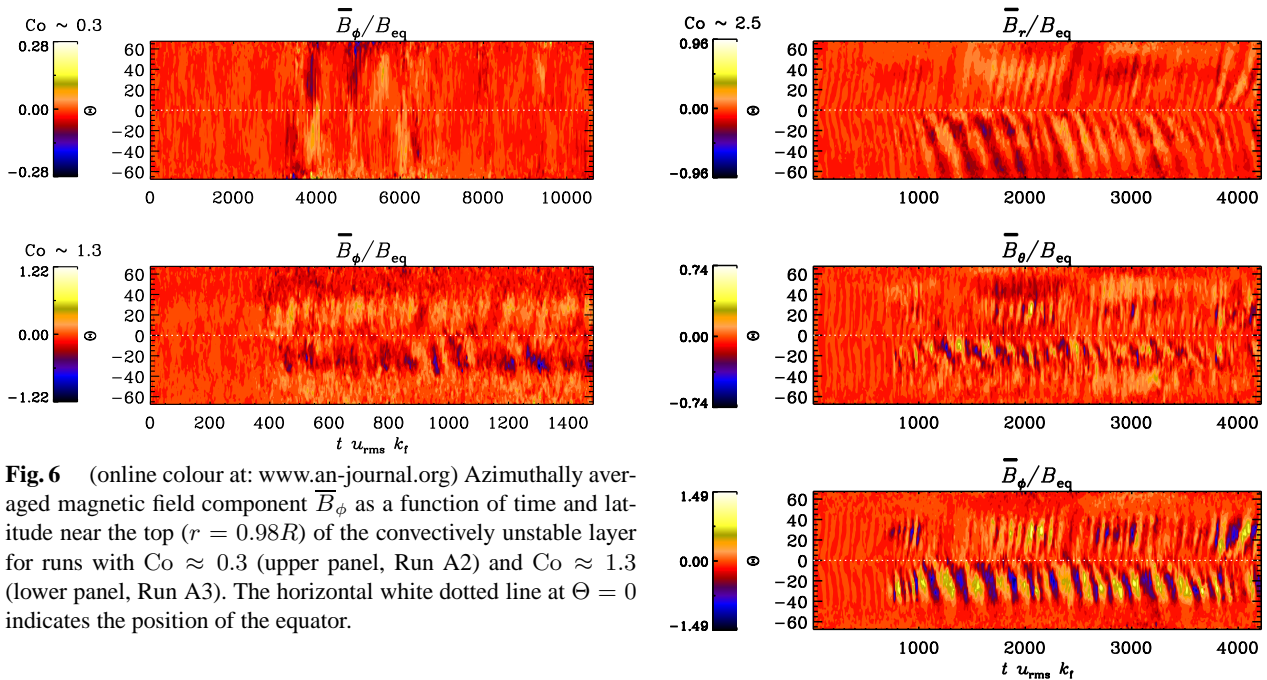

Fig. 6 (online colour at: www.an-journal.org) Azimuthally averaged magnetic field component $\overline{B}_\phi$ as a function of time and latitude near the top ($r = 0.98R$) of the convectively unstable layer for runs with Co ≈ 0.3 (upper panel, Run A2) and Co ≈ 1.3 (lower panel, Run A3). The horizontal white dotted line at $\Theta = 0$ indicates the position of the equator.

Fig. 7 (online colour at: www.an-journal.org) Magnetic field components $\overline{B}_r$ (top panel), $\overline{B}_\theta$ (middle), and $\overline{B}_\phi$ (bottom) averaged over the azimuthal direction as a function of time and latitude near the top ($r = 0.98R$) of the convectively unstable layer from Run A4.

posite to that of the kinetic helicity, we would thus expect α to have a positive (negative) value in the northern (southern) hemisphere. Furthermore, there is a positive $d\Omega/dr$ near the equator, which leads to $\alpha\, d\Omega/dr > 0$ which, based on mean-field theory, should lead to poleward migration (e.g. Yoshimura 1975). We note that similar results were reported by Gilman (1983). However, a more detailed interpretation of the origin of the dynamo requires a better understanding of the turbulent transport coefficients.

We note that in the kinematic stage of the simulation the period of the oscillations is well-defined and the sign

changes occur nearly similarly on both hemispheres. In the saturated stage the oscillation period is expected to become slightly longer when the implied turbulent diffusion is quenched by the magnetic field (e.g. Käpylä & Brandenburg 2009). Such behaviour is indeed observed, but it appears
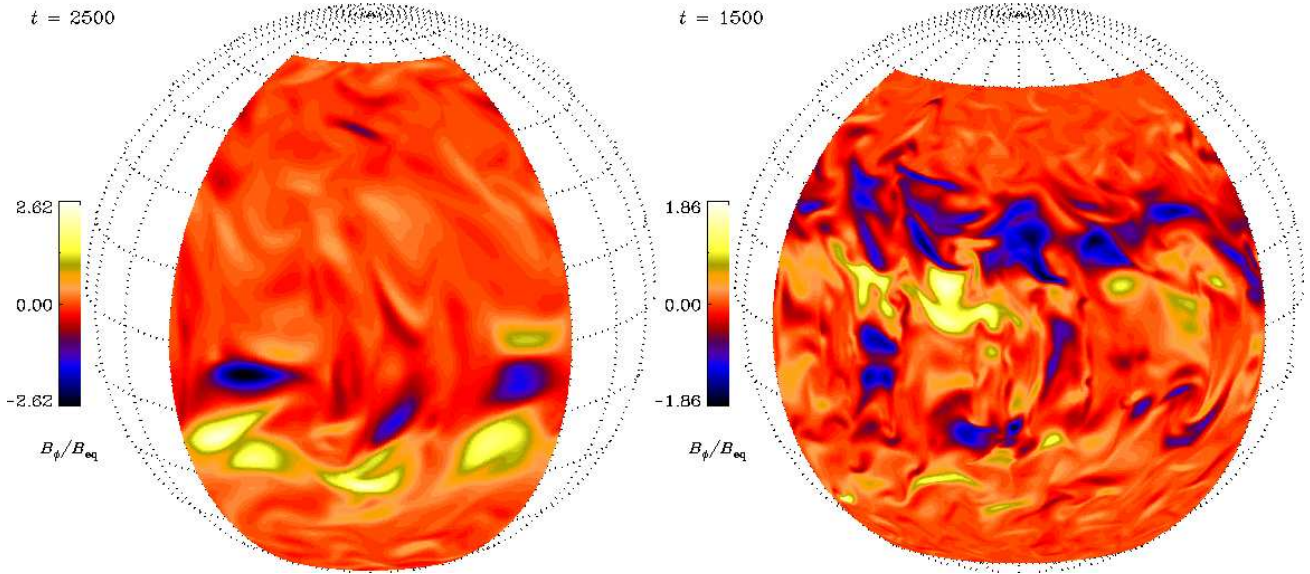
Fig. 10   (online colour at: www.an-journal.org) Toroidal magnetic field B_ϕ near the upper boundary ($r = 0.98R$) from the Runs A4 (left) and B1 (right).
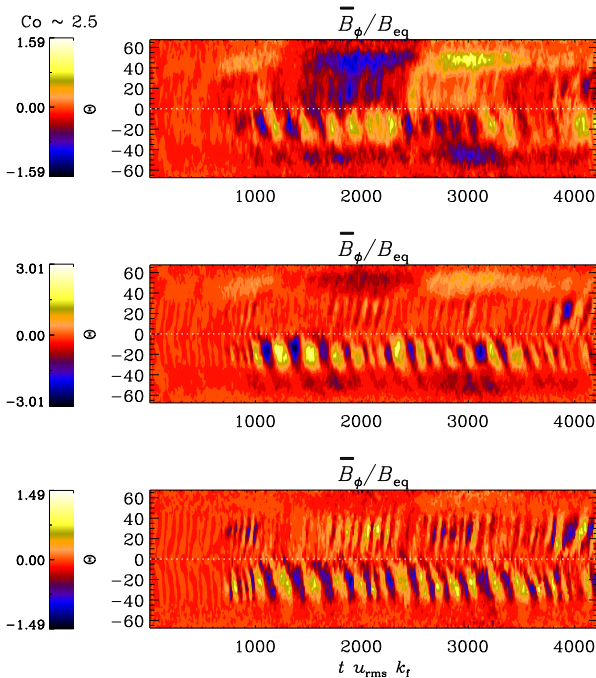

Fig. 9   (online colour at: www.an-journal.org) Magnetic field component $\overline{B}_\phi$, averaged over the azimuthal direction as a function of time and latitude from the bottom (top panel, $r = 0.7R$), middle (middle panel, $r = 0.85R$) and near the top (bottom panel, $r = 0.98R$) of the convectively unstable layer from Run A4.

that the two hemispheres begin to show a distinct asymmetry with different oscillation periods and magnitudes of the fields in the saturated state (see Figs. 7, 8, and 10). We note that hemispherical dynamos, where one of the hemispheres is almost devoid of magnetic fields, have been reported from rapidly rotating spherical shells (Grote & Busse 2000; Busse 2002). These dynamos also exhibit poleward

migration of activity belts similar to the results reported here. Furthermore, Fig. 9 shows that in the deeper layers the magnetic field has a very different structure with strong large-scale fields reaching much higher latitudes that can also change sign, but more irregularly and on a time scale that is much longer than that shown by the field near the surface. Since the differential rotation in these models is appreciable only near the equator, it is conceivable that there is a competition between different dynamo modes in the deeper layers and those at the higher latitudes and that the irregular nature of the oscillations in the saturated state is caused by the interaction between these regions.

4   Conclusions

In this paper we have presented preliminary results of rotating turbulent convection in spherical wedge geometry for different rotation rates. We find that for small values of the Coriolis number the differential rotation is anti-solar, with the equator rotating slower in comparison to higher latitudes. When the Coriolis number is increased above unity, the rotation profile changes to a more solar-like configuration with faster rotation at the equator and slower rotation at higher latitudes. However, with more rapid rotation ($\mathrm{Co} \gtrsim 1$) the Taylor-Proudman balance dictates the rotation profile with contours that tend to be constant along cylinders.

The same setup is used to study the corresponding dynamo solutions. The magnetic Reynolds number is chosen such that there is no dynamo in the absence of rotation. A dynamo is excited for sufficiently rapid rotation. Near the marginally excited state the magnetic energy is only roughly ten per cent of the kinetic energy, but a large-scale structure can already be observed. With more rapid rotation

($Co \gtrsim 1$), strong large-scale magnetic fields are obtained. In this case the field is non-oscillatory. Increasing the rotation rate further changes the solution such that an oscillatory magnetic field is observed near the equator in the upper parts of the convectively unstable layer. The magnetic features appear at low latitudes and propagate poleward, i.e. opposite to the behaviour seen in the Sun. However, the kinetic helicity in this run suggests that the α effect is positive (negative) in the northern (southern) hemisphere. This together with the positive radial gradient of Ω near the equator is consistent with a dynamo wave propagating poleward.

Our model is in some ways similar to that of Gilman (1983) which also omitted the regions near the pole and used the same boundary conditions for the magnetic field. The main difference between our models is that we include density stratification and add a lower overshoot layer. Many of the results, e.g. a poleward propagating dynamo wave in our most rapidly rotating runs, are qualitatively similar to those found by Gilman (1983). However, we obtain a deep-seated non-oscillatory field and see large differences in the activity levels on different hemispheres which were not reported by Gilman. The differences between the setups could explain some of the discrepancies of the results.

Our ultimate aim with this model is to study dynamo processes that operate in solar and stellar interiors. In order to achieve this goal we need to find a way to break the Taylor-Proudman balance. A possible solution would involve the inclusion of subgrid scale anisotropic turbulent heat transport in the model. It is also unclear how the introduction of latitudinal boundaries affects the large-scale behaviour of the solutions. Issues related to these problems will be dealt with in future publications.

References

Brandenburg, A., Subramanian, K.: 2005, PhR 417, 1

Brandenburg, A., Moss, D., Rüdiger, G., Tuominen, I.: 1991, GApFD 61, 179

Brandenburg, A., Jennings, R.L., Nordlund, Å., et al.: 1996, JFM 306, 325

Brandenburg, A., Käpylä, P.J., Mitra, D., Moss, D., Tavakol, R.: 2007, AN 328, 1118

Brandenburg, A., Rädler, K.-H., Rheinhardt, M., Käpylä, P.J.: 2008, ApJ 676, 740

Brown, B.P., Browning, M.K., Brun, A.S., et al.: 2007, in: R.J. Stancliffe, G. Houdek, R.G. Martin, C.A. Tout (eds.), *Unsolved Problems in Stellar Physics: A Conference in Honor of Douglas Gough*, AIPC 948, p. 271

Brown, B.P., Browning, M.K., Brun, A.S., Miesch, M.S., Toomre, J.: 2008, ApJ, 689, 1354

Brown, B.P., Browning, M.K., Miesch, M.S., Brun, A.S., Toomre, J.: 2009, ApJ, submitted, astro-ph/0906.2407

Browning, M.K., Miesch, M.S., Brun, A.S., Toomre, J.: 2006, ApJ 648, L157

Brun, A.S., Miesch, M.S., Toomre, J.: 2004, ApJ 614, 1073

Busse, F.: 2002, PhFl 14, 1301

Cattaneo, F., Hughes, D.W.: 2006, JFM 553, 401

DeRosa, M.L., Hurlburt, N.E.: 2003, in: S. Turcotte, S.C. Keller, R.M. Cavallo (eds.), *3D Stellar Evolution*, ASPC 293, p. 229

Dobler, W., Stix, M., Brandenburg, A.: 2006, ApJ 638, 336

Durney, B.R., Roxburgh, I.W.: 1971, SoPh 16, 3

Gilman, P.A.: 1983, ApJS 53, 243

Glatzmaier, G.A.: 1985, ApJ 291, 300

Grote, E., Busse, F.: 2000, PRE 62, 4457

Hughes, D.W., Proctor, M.R.E.: 2009, PRL 102, 044501

Jones, C.A., Roberts, P.H.: 2000, JFM 404, 311

Käpylä, P.J., Brandenburg, A.: 2009, ApJ 699, 1059

Käpylä, P.J., Korpi, M.J., Ossendrijver, M., Stix, M.: 2006, A&A 455, 401

Käpylä, P.J., Korpi, M.J., Brandenburg, A.: 2008, A&A 491, 353

Käpylä, P.J., Korpi, M.J., Brandenburg, A.: 2009a, ApJ 697, 1153

Käpylä, P.J., Korpi, M.J., Brandenburg, A.: 2009b, A&A 500, 633

Käpylä, P.J., Korpi, M.J., Brandenburg, A.: 2009c, MNRAS, in press, astro-ph/0908.2423

Kitchatinov, L.L., Pipin, V.V., Rüdiger, G.: 1994, AN 315, 157

Krause, F., Rädler, K.-H.: 1980, *Mean-field Magnetohydrodynamics and Dynamo Theory*, Pergamon Press, Oxford

Miesch, M.S., Elliott, J.R., Toomre, J., et al.: 2000, ApJ 532, 593

Miesch, M.S., Brun, A.S., Toomre, J.: 2006, ApJ 641, 618

Mitra, D., Tavakol, R., Brandenburg, A., Moss, D.: 2009a, ApJ 697, 923

Mitra, D., Tavakol, R., Käpylä, P.J., Brandenburg, A.: 2009b, astro-ph/0901.2364

Moffatt, H.K.: 1978, *Magnetic Field Generation in Electrically Conducting Fluids*, Cambridge Univ. Press, Cambridge

Nordlund, Å., Brandenburg, A., Jennings, R.L., et al.: 1992, ApJ 392, 647

Ossendrijver, M.: 2003, A&ARv 11, 287

Rädler, K.-H.: 1980, AN 301, 101

Robinson, F.J., Chan, K.L.: 2001, MNRAS 321, 723

Rogachevskii, I., Kleeorin, N.: 2003, Phys Rev E 68, 036301

Rogachevskii, I., Kleeorin, N.: 2004, Phys Rev E 70, 046310

Rotvig, J., Jones, C.A.: 2002, Phys Rev E 66, 056308

Rüdiger, G., Hollerbach, R.: 2004, *The Magnetic Universe*, Wiley-VCH, Weinheim

Rüdiger, G., Egorov, P., Kitchatinov, L.L., Küker, M.: 2005, A&A 431, 345

Schrinner, M., Rädler, K.-H., Schmitt, D., et al.: 2005, AN 326, 245

Schrinner, M., Rädler, K.-H., Schmitt, D., et al.: 2007, GApFD 101, 81

Yoshimura, H.: 1975, ApJ 201, 740

Yousef, T.A., Heinemann, T., Schekochihin, A.A., et al.: 2008a, PRL 100, 184501

Yousef, T.A., Heinemann, T., Rincon, F., et al.: 2008b, AN 329, 737